Spectroscopic modeling and characterization of a collisionally confined laser-ablated plasma plume

M. E. Sherrill,[1,*] R. C. Mancini,[1] J. Bailey,[2] A. Filuk,[2] B. Clark,[2] P. Lake,[2] and J. Abdallah, Jr.[3]
[1]*Department of Physics, University of Nevada, Reno, Nevada 89557, USA*
[2]*Sandia National Laboratories, Albuquerque, New Mexico 87185, USA*
[3]*Theoretical Division, Los Alamos National Laboratory, Los Alamos, New Mexico 87545, USA*
(Received 11 May 2007; published 6 November 2007)

Plasma plumes produced by laser ablation are an established method for manufacturing the high quality stoichiometrically complex thin films used for a variety of optical, photoelectric, and superconducting applications. The state and reproducibility of the plasma close to the surface of the irradiated target plays a critical role in producing high quality thin films. Unfortunately, this dense plasma has historically eluded quantifiable characterization. The difficulty in modeling the plume formation arises in the accounting for the small amount of energy deposited into the target when physical properties of these exotic target materials are not known. In this work we obtain the high density state of the plasma plume through the use of an experimental spectroscopic technique and a custom spectroscopic model. In addition to obtaining detailed temperature and density profiles, issues regarding line broadening and opacity for spectroscopic characterization will be addressed for this unique environment.

DOI: 10.1103/PhysRevE.76.056401 PACS number(s): 52.38.Mf, 52.50.Jm, 52.77.−j

I. INTRODUCTION

Laser ablation refers to the process of ablating material from a solid or liquid target with a low intensity laser ranging from 1×10^7 W/cm^2 to 1×10^{10} W/cm^2. It deposits the bulk of its energy in the skin depth region of the target, where this volume of material is heated and then undergoes melting, evaporation, and possibly plasma formation. The material in the gaseous state then forms a plume that expands away from the target's surface with normal to the surface velocities of a few 10 μm/ns.

Laser ablation is commonly used in both experimental physics as ion sources and in industry for the generation of thin films. In fact, laser ablation has proved to be the most consistent method of producing high quality thin films, in particular for stoichiometrically complex materials. This technique has been used in the manufacturing of electronic and optical films, superconductors, ferroelectrics, piezoelectrics, and photoelectric materials as well as tribological coatings such as diamondlike thin films [1–3].

Work that has attempted to describe ablation physics, in general, has resided either in the detailed modeling of laser target interactions [4] or the modeling of the expanded plume through gas dynamic simulations [5–7] or hybrid models [8]. Interestingly, a detailed study of the plasma in the region between the target and a few millimeters from the target has not been undertaken [9], although it is this region of the plasma that defines the level populations and the ionization abundances of the plasma far away and later in time (in the absence of background gases).

The difficulty in modeling the plume formation arises in the accounting for the small amount of laser energy that is deposited on the target. Poor knowledge about temperature-dependent reflectivity and conductivity as well as the equation of state of these exotic materials makes simulations very impractical.

The goal of this work was to develop both experimental and modeling techniques to spectroscopically characterize moderately complex laser-ablated plasma plumes for the region a few tens of microns away from the target surface and early in time (20–30 ns after the end of the laser pulse). To this end, an innovative experimental technique was developed to reduce plasma gradients in order to simplify the interpretation and spectroscopic analysis. Both temporally and spatially resolved visible spectra was recorded during this experiment. Several high-temperature spectral modeling techniques historically employed to quantitatively describe the detailed state of plasmas [10] have been employed in this work. In addition, modeling techniques have also been developed to deal with the specific issues unique to modeling ablation plasmas.

II. EXPERIMENTAL DESIGN AND DETAILS

In a series of experiments performed at Sandia National Laboratories (SNL), a binary alloy target composed of 47% Li and 53% Ag was irradiated using a Nd YAG laser with a Gaussian pulse of 10 ns, at an angle of incidence of 30° to the target's normal and a fluence of 0.7 J/cm^2 which corresponds to an intensity of 1×10^8 W/cm^2.[1] Time and spatially resolved (along the direction normal to the target's surface) optical spectra in the 4000–7000 Å range were recorded with a framing spectrograph. In order to limit the effects of plasma gradients on the spectra due to lateral expansion along a direction perpendicular to the target's normal, a tar-

*Current address: Theoretical Division, Los Alamos National Laboratory, Los Alamos, New Mexico 87545, USA.

[1]The Li-Ag binary alloy used in this work is an idealization of the mixed mid- and low-Z materials often seen in thin film manufacturing such as the high-temperature superconductor, $Y_1Ba_2Cu_3O_x$.

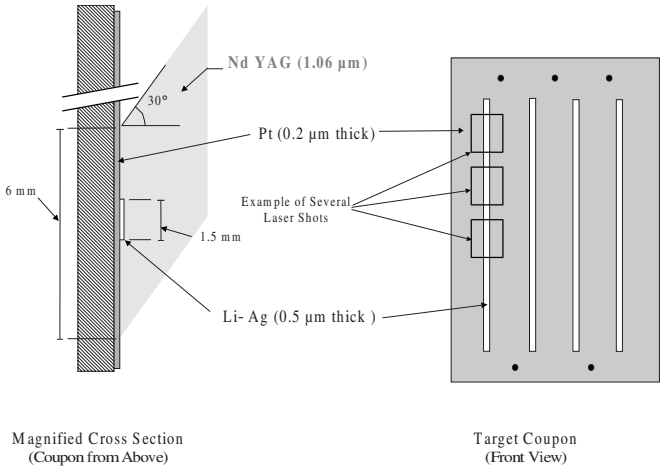

FIG. 1. Target design.

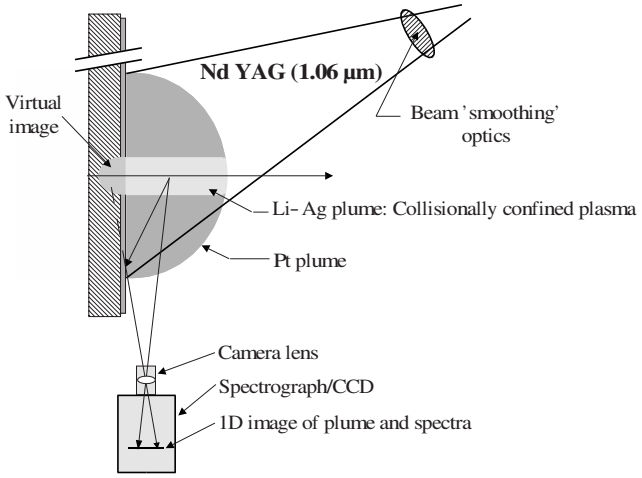

FIG. 2. Experimental configuration—view from above.

get design and instrument were implemented. Several 1.5-mm-wide, 0.5-μm-thick thin film strips of Li-Ag were coated on top of a 0.2-μm-thick Pt-coated substrate. The 6 $\times 6$ mm^2 square laser focal spot illuminated both the Li-Ag strip and the surrounding Pt base, as illustrated in Fig. 1. During the expansion of the metallic plume, the Pt plasma collisionally confined the Li-Ag core, thus reducing the Li-Ag lateral expansion as schematically illustrated in Fig. 2.[2] This technique represents a variation on the microdot spectroscopy method commonly employed in x-ray spectroscopy of high-temperature laser-produced plasmas [11], and it permitted a more accurate characterization of the Li-Ag plasma plume by reducing plasma gradients along the line of sight of the spectrometer. A package of laser-beam smoothing optics, based on a diffuser and homogenizer, was used to improve the laser irradiation uniformity on the target. A gated spectrograph equipped with an f5.6 Nikon lens and a 159 g/mm diffraction grating coupled to a charged coupled device (CCD) was set up to record a time-resolved one-dimensional (1D) image along the target's normal direction, i.e., a single time snapshot with a 1D spatial image. The depth of field of the lens was used to image the Li-Ag plasma, thus minimizing contributions from the Pt portion of the plasma. Each data image was integrated over a 2 ns time interval, and multiple shots with the spectrometer triggered at 10, 20, 30, 40, 50, 75, and 100 ns after the end of the laser pulse were recorded to construct the spectral time history as seen in Fig. 3. Spatial resolution was approximately 60 μm, while the spectral resolution power was 600 ($\lambda/\delta\lambda$).

As illustrated in Fig. 3, the horizontal axis of each CCD image represents the wavelength range of 4000–7000 Å, while the vertical axis represents the distance from and normal to the surface of the target from -2100 μm to $+2100$ μm, i.e., $x=0$ characterizes the location of the target's surface. The instrument recorded the real as well as the virtual image due to the reflection of the plume emission from the mirrorlike surface of the target (see diagram in Fig. 2). Early in time, only continuum emission is observed. Later, the images display characteristic line emissions from transitions in Li and Ag atoms. First, the line emissions are localized close to the surface and the lines are broad. This suggests the formation of a dense surface plasma. For later times, the spatial intensity distributions move away from the surface and the lines become narrower. This is a clear indication of the plasma plume expansion.

A. Intensity and spatial calibration

To calibrate both the intensity and spatial dimension of the imaging spectrograph, a well-characterized light source smaller than the spectrograph's field of view was created. The end of a 100 μm diameter light emitting fiber-optic line was chosen as the light source. A bright 500 W Xe arc lamp with collecting optics fed the optical fiber. The goal was to record absolute spectra of the plasma. To accomplish this, two separate measurements were needed to characterize this light source.

The first step toward characterization constituted measuring the output of the source with an absolutely calibrated photodiode in conjunction with seven separate 100 Å wide bandpass filters. Though the data recorded from these measurements were absolute, they were of coarse spectral resolution. A second set of relative measurements was performed with a much higher spectral resolution. A NIST traceable lamp was used to calibrate the relative spectral sensitivity of a line spectrograph. Following this calibration, light from the fiber optic source was then recorded. This output as a function of wavelength would then be scaled with the calibrated photodiode data to produce absolute power as a function of wavelength.

To calibrate the framed spectrograph, including the effect of collection optics, the end of the fiber optic source was placed at the location where the plasma would be generated. From the gated time images (2–500 ns) of the fiber source, the CCD pixel to spatial scale factor was determined

[2]The Li-Ag column is in pressure equilibrium with the confining Pt plasma. Pt was specifically selected for its ability to absorb the laser radiation at the same rate as the Li-Ag stripe, thereby assuring that the surrogate (Li-Ag, Pt) and pure (Li-Ag) plasmas have the same hydrodynamic behavior. The consistency of the column was validated by two-dimensional imaging.

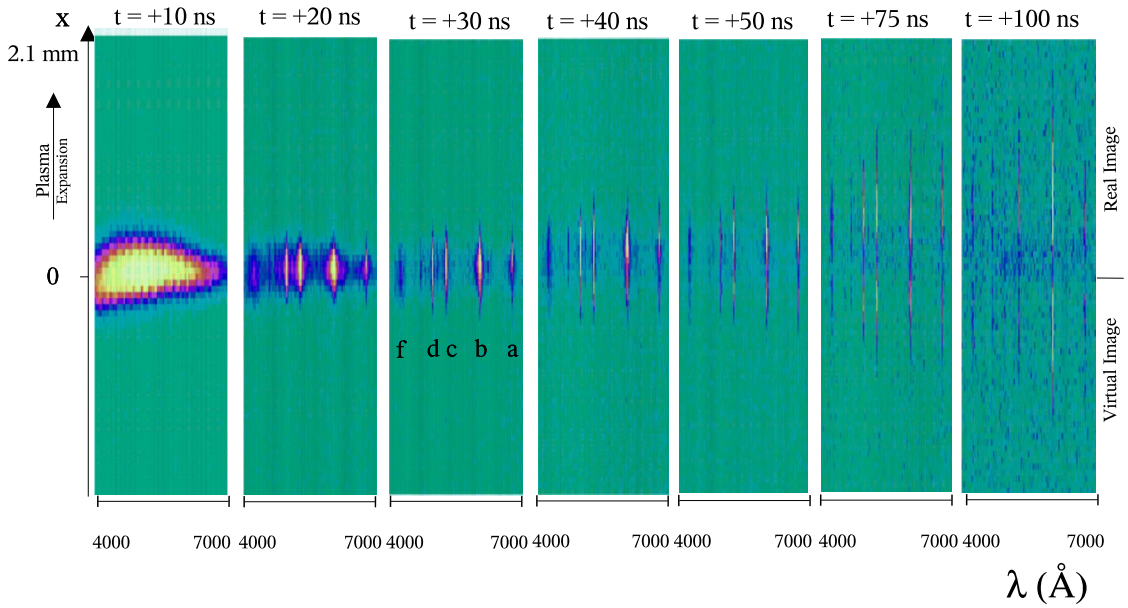

FIG. 3. (Color online) Experimental CCD images recorded at 0, 20, 30, 40, 50, 75, and 100 ns after the end of the laser pulse. Vertical axis represents the spatial expansion of the plasma perpendicular to the target's surface.

(57.6 μm/pixel) as well as the total system efficiency. The data obtained from lineouts taken along the spectral axis of the CCD images were ultimately divided by the total system efficiency. Though a calibrated source was produced and the efficiency of the framing spectrograph was determined, differences still existed between the absolute experimental spectra and synthetic spectra. These differences can be attributed, in part, to uncertainties in the collection angles. A Ne ORIEL spectral lamp was used in the wavelength calibration of the framing spectrograph. This lamp provided several well-defined lines within the region of spectral interest (4000–7000 Å).

III. TIME- AND SPACE-RESOLVED LINEOUTS

Spatially resolved spectral lineouts can be extracted from the data images. Early in time and close to the surface (Fig. 4) the spectrum is dominated by neutral Li and Ag spectral features (see Table I for line identification). The g feature is composed of both a broadened forbidden transition arising from Stark mixed energy levels and a possible $4d^8 5s^2(^3F_2)$-$4d^9 5p(^3P_1)$ transition in Ag II.[3] Due to the high plasma density, line shapes exhibit Stark, resonance and opacity broadening. Furthermore, the Li $3d$-$2p$ line displays a self-reversal feature due to opacity effects, which lends evidence that a slight gradient in the density still exists after collisional confinement by the platinum. In this figure we also see the signal of hydrogen, a contaminant. Later in time and away from the surface, line shapes are dominated by the characteristic instrumental function. From the 100 ns spectral lineouts, the average full width at half-maximum (FWHM) of the Li I: $1s^2 3d$-$1s^2 2p$ was measured to be 0.004 11 eV and this value was used as an estimate of the instrumental resolution function.

Though the nonplatinum core of the plasma was imaged, platinum lines are still observed in the Li-Ag spectrum (Fig. 5). A pure platinum target was irradiated and its spectrum recorded. Since a large number of Pt lines reside in the f (in Fig. 5) spectral feature this region does not lend itself for use in diagnosing the state of the core plasma. Also, platinum contributions to both the silver $5d$-$5p$ (c in Fig. 5) and the lithium $2s$-$2p$ (a in Fig. 5) lines are present. A comparison between the two spectra can only be used for determining the location of some Pt lines. Plasma conditions differ greatly between the two systems making it difficult to predict the amount of Pt contributions in the above-mentioned lines. Pt line identification is unknown at this time since nearly all energy levels in neutral platinum remain unidentified.

IV. ATOMIC DATA FOR NEUTRALS AND LOW-CHARGE IONS OF Li AND Ag

A synthetic spectrum is sensitive to the atomic structure and collision cross-section data when the plasma is not in thermal equilibrium. Due to the nature of the laser ablation with respect to their use in industrial applications, targets are often composed of compounds containing transition elements with $3d^w$, $4d^w$, $4f^w$, and $5f^w$ outer spin orbitals for their ground state configuration. Elements such as these pose a considerable challenge in calculating spectroscopically accurate neutral atomic energy levels as well as wave functions needed in collisional cross sections and line profile calculations.

Figure 6 illustrates the discrepancies between experimentally obtained Ag energy levels [12,13] and those computed

[3]Since fine-structure line transitions in Ag II were not resolved in the synthetic spectral model, the intensity of the $4d^8 5s^2(^3F_2)$-$4d^9 5p(^3P_1)$ transition was not computed, though its spectral line position corresponds to the experimental feature.

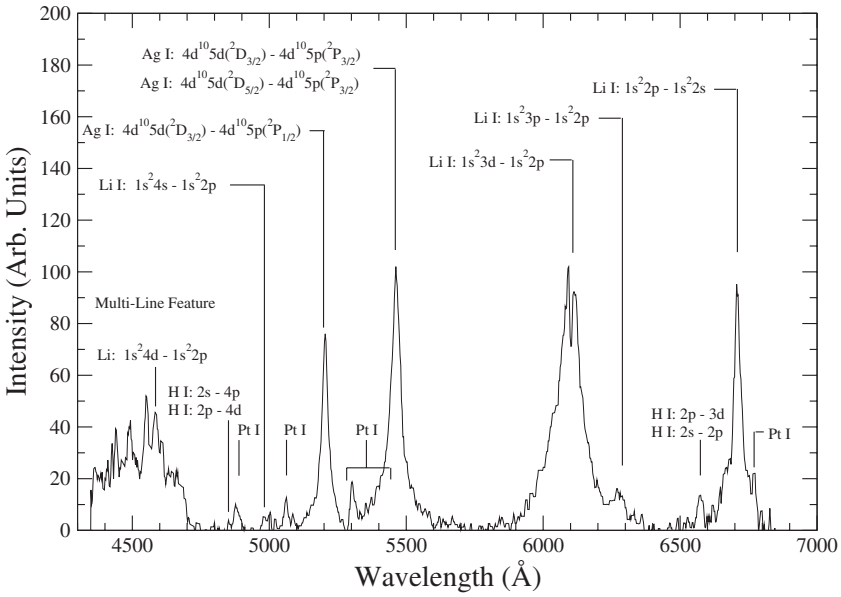

FIG. 4. Early in time and close to the target surface, this lineout (x=28.8 μm, t=+20 ns) displays the high density characteristics of Stark broadened line shapes.

by the Hartree-Fock atomic structure code, CATS [14]. This figure displays the typical compression in the computed atomic structure of transition elements such as Ag, with a comparison to the experimental values. Electron-electron correlation and relativistic corrections have been included in the calculations. In addition, a closer inspection of Fig. 6 reveals an inconsistent ordering of calculated energy levels with respect to experimental values. Both the compression and the incorrect ordering of calculated energy levels make this CATS data inappropriate for spectroscopic modeling. To correct the energy levels structure and their associated wave functions, the RCE procedure was used [15]. The RCE procedure varies the radial energy parameters in an iterative and interactive fashion with a least-square fit to experimentally obtained energy levels. The newly obtained radial energy parameters are then used to obtain the corrected wave functions. These wave functions are then used by two LANL codes[4] to compute electron impact excitation cross sections, ACE, [16] and electron impact ionization cross sections. Both codes computed cross sections in the distorted wave approximation.

The RCE procedure produced energy eigenvalues to five significant figures of the experimental data found for neutral silver. The comparisons between ACE excitation cross sections with and without RCE improved wave functions varied. The largest cross sections underwent a reduction as great as 13% as seen in the Ag I $4d^{10}5s^2S_{1/2}$-$4d^{10}5p^2P_{1/2}$ transition, while others produced only minor changes as seen in the Ag I $4d^{10}5p^2P_{1/2}$-$4d^{10}5p^2P_{1/2}$ transition of Fig. 7. In a similar manner, some small cross sections underwent a more drastic change with some values increasing. Though these changes in cross sections may not appear significant, they do lead to significant changes in the corresponding rate as seen in Fig. 8, in particular for the low electron temperatures found in ablation plasmas.

[4]http://aphysics2.lanl.gov/tempweb/

V. ATOMIC KINETICS OF Li-Ag PLASMA PLUMES

Due to the complexity of the materials of modern microelectronics, one commonly finds multielement laser-ablation targets with nearly equal abundances of each element. This implies that the atomic kinetics of this type of plasma cannot be modeled by assuming that the level populations and ionization balance for each element in the plasma are weakly influenced by the other elemental species. For this research, an algorithm was developed to calculate level populations in ablation plasmas by including the effects between several species through their interaction with the common free-electron pool.

Similar to the common laser-ablation target mentioned above, the SNL target contained nearly equal abundances of Ag and Li, 57% and 43%, respectively. Due to their contrasting atomic structure, each element's fractional contribution to the total electron pool is strongly correlated to the temperature and density found for the ablation plasma. At low

TABLE I. Li, Ag, and Pt lines observed in the experiment.

Label	Atom	λ (Å)		Transition
a	Li	6709		$1s^22p$-$1s^22s$
g	Li/Ag II	~6250	Li	$1s^23p$-$1s^22p$, forbidden line
			Ag II	$4d^85s^2(^3F_2)$-$4d^95p(^3P_1)$
b	Li	6104		$1s^23d$-$1s^22p$
c	Ag	5470		$4d^{10}5d(^2D_{3/2})$-$4d^{10}5p(^2P_{3/2})$
				$4d^{10}5d(^2D_{5/2})$-$4d^{10}5p(^2P_{3/2})$
d	Ag	5211		$4d^{10}5d(^2D_{3/2})$-$4d^{10}5p(^2P_{1/2})$
e	Li	4972		$1s^24s$-$1s^22p$
f	Li/Ag/Pt	~4600	Li	$1s^24d$-$1s^22p$
			Ag	$4d^{10}7s$-$4d^{10}5p$, $4d^{10}8p$-$4d^95s^2$, $4d^{10}5f$-$4d^95s^2$
			Pt	$5d^86s^16p^1$-$5d^96s^1$

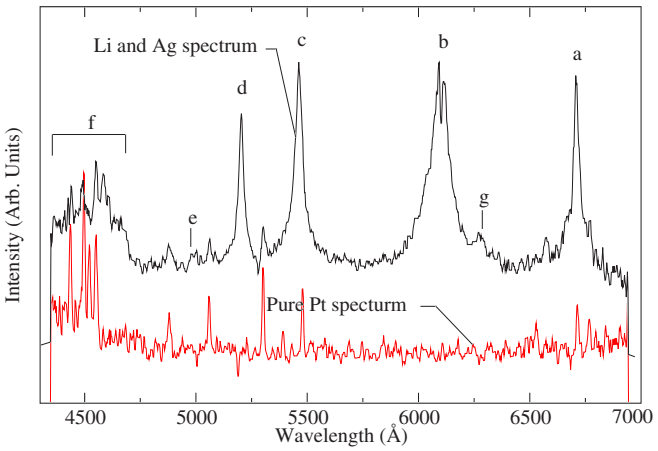

FIG. 5. (Color online) The superposition of two lineouts shows the location of platinum lines in the $x=28.8$ μm, $t=+20$ ns spectrum. The spectrum of a pure platinum target was recorded during the Li-Ag trials at $t=+50$ ns, $x=56.7$ μm from the surface with a 10 ns gate time.

temperatures (less than ~1 eV), Li is more ionized than Ag since the ionization potential of Li ($I_p=5.392$ eV) is smaller than that for Ag ($I_p=7.574$ eV). As the temperature increases from 1 eV to 3 eV, Ag atoms ionize and effectively populate states in Ag^{+1} and Ag^{+2}, while the population distribution of the Li states remains relatively unchanged and mainly accumulates in the Li^{+1} ion ground state due to the 60.9 eV transition energy needed for an excitation to the first excited state.

A. Atomic kinetic model

Our atomic kinetics model considers the neutral Ag atom and its first three ionization stages and the neutral Li atom and its first two ionization stages. Since the second ionization potential of Li is 75.6 eV (compared to 5.392 eV for the first ionization potential) and the range of relevant plasma temperatures is between 0.5 eV and 2.0 eV, very little population is expected to reside in the higher ionization stages of Li. In each atom (ion), ground and several excited states are

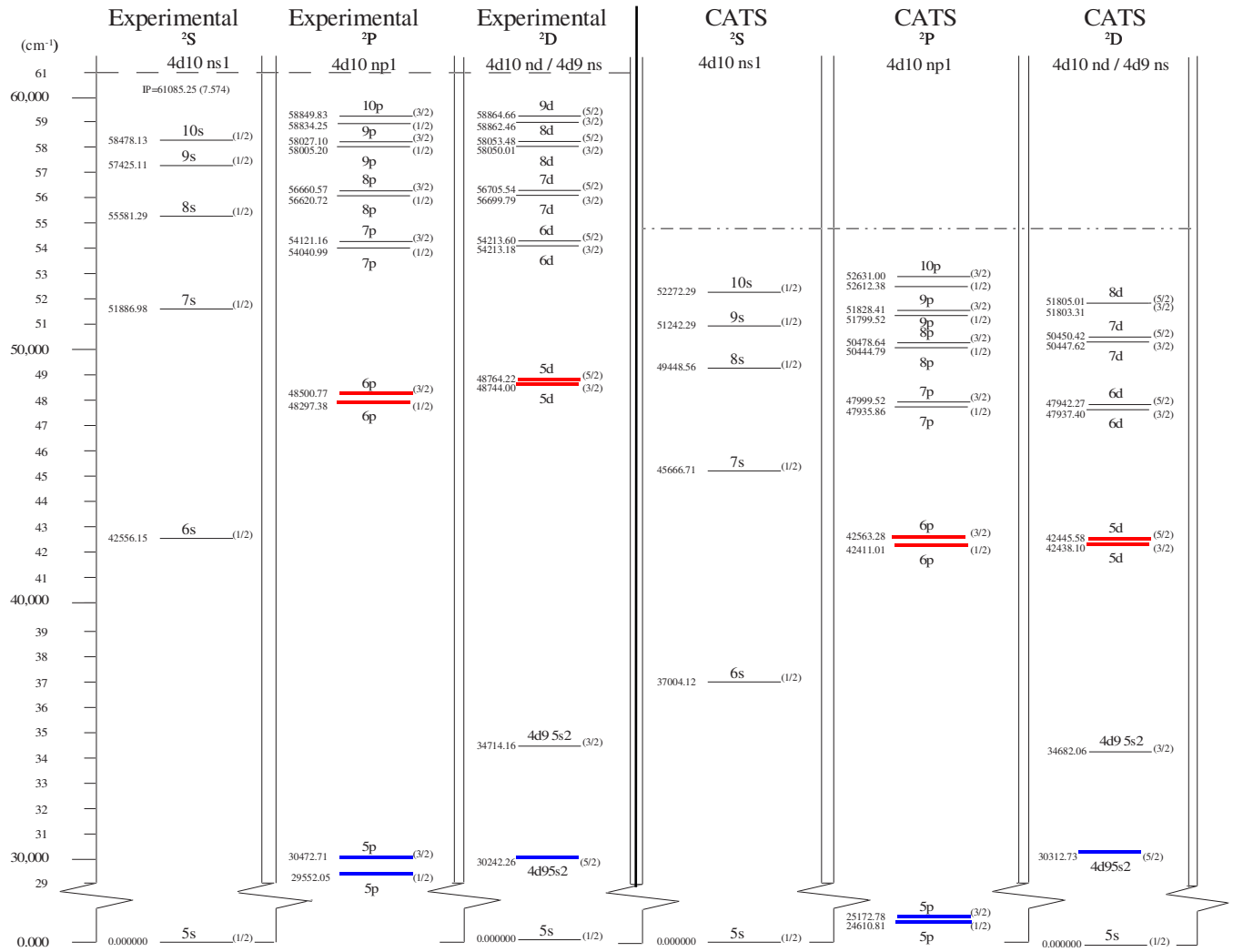

FIG. 6. (Color online) This comparison between experimentally obtained energy level structure (left-hand side) and energy levels generated with Cowan's atomic structure code (CATS) (right-hand side) for neutral Ag illustrates the compression of the energy level structure typically seen for mid-Z neutral atoms.

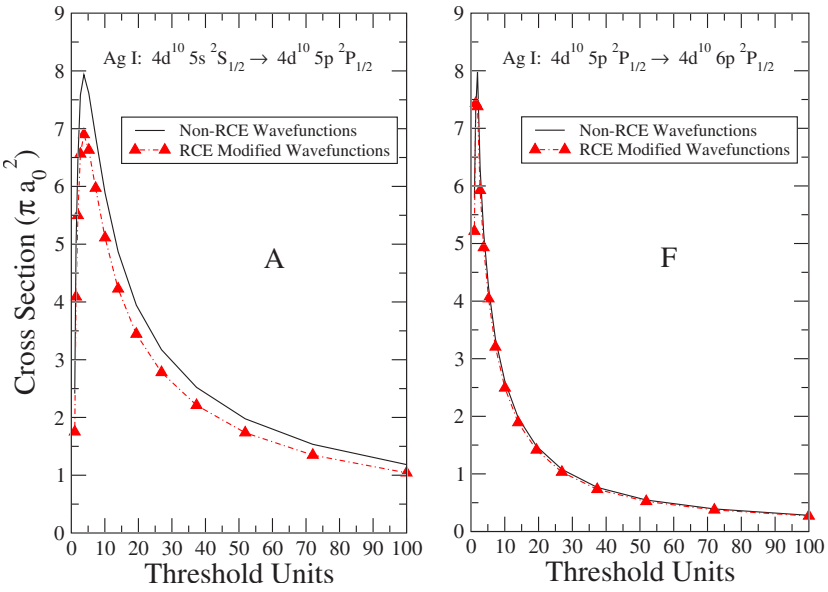

FIG. 7. (Color online) Comparison of electron impact excitation cross sections generated with and without RCE modifications of the wave functions. The two figures correspond to allowed (A) (left) and forbidden (F) (right) transitions.

considered, including some autoionization states. Fine-structure energy levels are used to describe excited states in dominant line transitions identified in the experimental spectra for the analysis. Configuration average energies are used for Ag^{1+} and Ag^{2+} ionization stages. This use of a coarser grain atomic structure representation for nonspectroscopically significant ionization stages in Ag arises from the compromise between having to include these ionization stages in the determination of the appropriate ionization balance, and overcoming the technical difficulty of representing the atomic stages of partially filled *d*-shell ions. See Table II for the energy level structure used in the model.

B. Assessing the existence of time-dependent atomic kinetics

To assess if time-dependent atomic kinetics would be required to model the early in time and close to the surface ablation plasma, temperature and density time histories would have to be obtained. We were unable to perform an *ab initio* simulation of the hydrodynamic expansion of the plasma plume, due to the lack of a detailed description of the temperature-dependent laser absorption properties of the LiAg alloy. However, we were able to perform a parameter study with a 1D hydrodynamic code[5] to produce a set of the temperature and density time histories consistent with a rough estimate of the plume expansion observed in the CCD images. A time-dependent collisional-radiative model driven by these time histories did not produce results that differed, to any significant degree, from those obtained by the steady state model. However, for the more rarefied cases of 50 and 75 ns at 170 and 450 μm, respectively, this study and the experimental spectra did suggest the existence of time-dependent atomic kinetics [17].

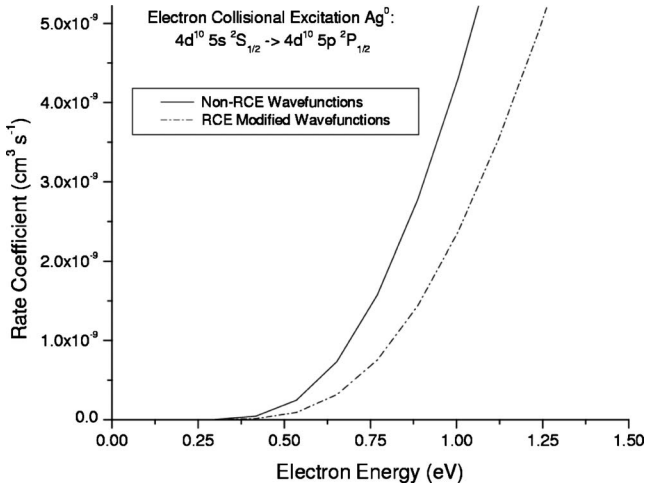

FIG. 8. A comparison of an electron impact excitation rate for silver generated with and without wave-function modifications by the RCE procedure.

C. Single element atomic kinetic model

In a single element plasma, the atomic kinetic model constitutes N rate equations that describe the rate of change of the fractional population for each level (f_n), where N is the total number of energy levels included in the kinetic model. The set of equations may be represented in matrix form as

$$\frac{d\boldsymbol{f}}{dt} = A\boldsymbol{f}. \tag{1}$$

For the special case of a plasma in steady state, the population of the levels remains constant, or more precisely, $df_n/dt=0$ for all n. Unfortunately, the equations represented in Eq. (1) are not linearly independent. To solve for the populations, the fractional normalization condition $\Sigma_{n=1}^{N} f_n = 1$ is substituted for one of the df_n/dt rate equations, resulting in the new expression, $A'\boldsymbol{f}=\boldsymbol{b}$. Multiplying both sides of this equation with the inverse of A' we obtain

$$\boldsymbol{f} = [A']^{-1}\boldsymbol{b}. \tag{2}$$

[5]A realistic equation of state for our LiAg alloy was produced (by J.D. Johnson of Los Alamos National Laboratory) for this work.

TABLE II. Detailed ionization and energy level structure of lithium and silver included in the atomic kinetic model.

Element	Ionization stage	Number of levels	Largest principal quantum number	Representation
Li	I	36	7	Levels
Li	II	22	7	Levels
Li	III	1	1	Levels
Ag	I	44	10	Levels
Ag	II	32	10	Configuration
Ag	III	32	10	Configuration
Ag	IV	1	1	Configuration

Several collisional and radiative atomic processes are included in the atomic kinetic model discussed above, namely, electron collisional excitation and deexcitation, electron collisional ionization and recombination, dielectronic recombination [18], spontaneous radiative decay and photoexcitation, radiative recombination and photoionization and multiphoton ionization [19]. Atomic rates associated with these processes are used to compute the matrix elements for the matrix **A** in the set of equations in Eq. (2). Ground and excited states of adjacent ionization stages are fully coupled through these atomic processes.

To account for nonideal plasma effects on the atomic kinetics, an additional correction was included to determine the degree of continuum lowering, i.e., the lowering of the ionization potential due to the plasma environment and in turn the removal of bound excited states from the energy level structure. This effect was approximated by the Stewart and Pyatt model [20]. The reduction of the ionization potential as a function of temperature and density requires an independent estimate of the average ionization stage. This was provided by an algorithm based on fitted and scaled results of the Thomas-Fermi model [21].

D. Multielement atomic kinetic model

The interactions between species are limited to those that occur through the pool of free electrons. For the steady state plasma, the calculations begin with the input of the total atom number density, N_a, and the electron temperature, T_e. From an initial estimate of $\bar{Z}^{\mathrm{Li}}$ and $\bar{Z}^{\mathrm{Ag}}$ and the atom number density, the electron number density, N_e, is determined. T_e and N_e are then used to determine the rates for the individual rate matrices of each species. After solving for the populations of each species, the $\bar{Z}^i$ of each individual species is obtained. The $\bar{Z}^i$'s of each element in conjunction with the abundances of each element and the total atom number density, N_a, is used to compute a new N_e which is sent back to the single element atomic kinetic models for the production of new $\bar{Z}^i$'s. This process continues until all the fractional populations of each level of each element varies no more than a set tolerance from the previous self-consistent iteration (see Fig. 9).

VI. SYNTHETIC SPECTRA CALCULATIONS

Line emission produced in an ablation plasma is altered from the ideal by two distinct mechanisms: first, by the influence of the plasma microfield on the radiator due to either charged particles or induced fields from neighboring atoms that distort the radiator's atomic potential, and in turn, shift its energy levels, leading to the characteristic broadening of

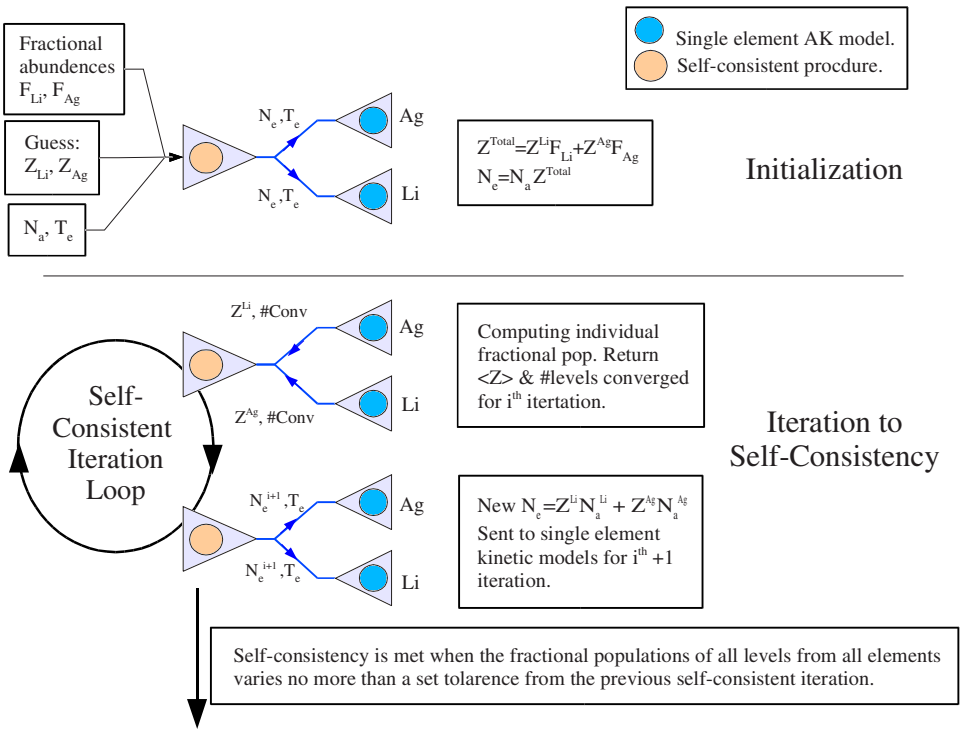

FIG. 9. (Color online) Multielement atomic kinetic model schematic diagram.

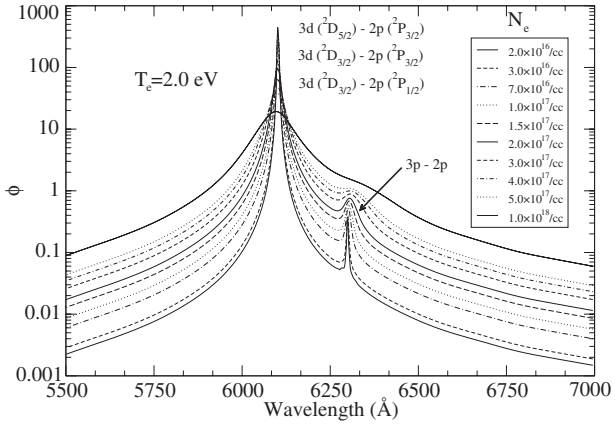

FIG. 10. Neutral lithium line profiles at various plasma electron densities for the dominant $3d$-$2p$ transition. Plasma microfield mixing of $1s^2 3p$ with $1s^2 3d$ energy level wave functions enhances the $1s^2 3p$ transition probability to the $1s^2 2p$ state, thereby producing the otherwise forbidden feature. Electron densities N_e (in units of cm^{-3}) are reported in the legend. Broader profiles are associated with greater electron density.

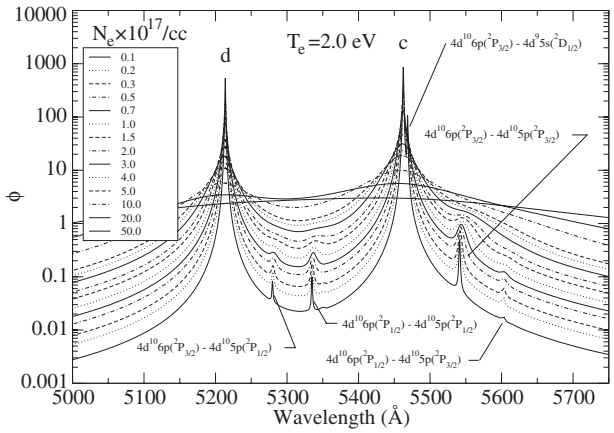

FIG. 11. Neutral silver line profiles for various plasma electron densities with the two dominant $5d$-$5p$ fine-structure transitions. Plasma microfield mixing of $4d^{10}6p$ with $4d^{10}5d$ energy level wave functions enhances the $4d^{10}6p$ transition probability to the $4d^{10}5p$ states, thereby producing the four small forbidden features. Also the low probability $4d^{10}6p$-$4d^9 5s$; $2e^-$ transition is present on the low energy side of line c. Electron densities N_e (in units of cm^{-3}) reported in the legend have been rescaled by 1×10^{17}. Broader profiles are associated with greater electron density.

the line profile; second, by the influence of the plasma opacity (line emission produced deep in a plasma must propagate through many plasma layers before escaping). Since photons at the center of the line emission are more efficiently absorbed than those in the wings, the line intensity distribution is distorted by the effects of radiation transport. These two effects must be taken into account when calculating synthetic spectra.

A. Line profile calculations

In this section, the line profile calculations of Li and Ag lines observed in the experimental spectra are discussed. Figures 10 and 11 display Stark-broadened line profiles for the Li $3d$-$2p$ and the two main Ag lines observed in the experimental spectra. The effect of the ions was calculated in the static ion approximation while that of the electrons was computed using a quantum-mechanical second-order relaxation theory [22,23]. The ion microfield distribution function was computed (and cross-checked for consistency) using both the APEX model [24] and the Tighe and Hooper model [25]. Since the energy separation between upper and lower energy level manifolds associated with these line transitions is not very large compared with the spread in energy within the manifolds, the usual nonquenching approximation was removed and full mixing between upper and lower manifolds by plasma microfields was included. Thus, for the Li line shapes mixing between fine-structure levels associated with $1s^2 2l$, $1s^2 3l$, $1s^2 4l$, and $1s^2 5l$ configurations was taken into account, and for the Ag line profiles $4d^{10}7s$, $4d^{10}6s$, $4d^{10}5s$, $4d^{10}7p$, $4d^{10}6p$, $4d^{10}5p$, $4d^{10}6d$, $4d^{10}5d$, $4d^9 5s^2$, and $4d^{10}4f$ were included.

The appearance of weak forbidden lines in the computed profiles is the result of plasma microfield mixing of energy levels. Field mixing affects those energy levels that lie closest together and mixes energy levels of opposite parity, in turn eliminating the total angular momentum and parity as good quantum numbers. Though these features are often small, they have the potential of being observed, since they often reside on the wings of larger spectral features and are not diminished by opacity effects of the bulk plasma.

An asymmetry in the series of profiles from low to high electron density may develop as in the case of the lithium $3d$-$2p$ profiles (Fig. 10). This asymmetry can be seen in the final synthetic spectral comparisons. In Fig. 11, the two $5d$-$5p$ fine-structure splitting spectral features of neutral silver are shown. These two lines are folded into a single profile. Included in the relative heights of this profile is an assumption of the relative populations of the upper levels. Due to the proximity in energy of the two upper levels to each other and the effect of collisions to thermalize these levels, we have assumed for the sake of generating this line shape that the ratio of their populations should follow from the ratio of their statistical weights.

B. Radiation transport

As introduced in Sec. III and will be further elaborated in Sec. VIII D, the evidence of the experimentally observed self-reversal feature in the Li: $3d$-$2p$ lineshape suggests the existence of plasma nonuniformities. Therefore we have included the capability of calculating gradients in the direction along the line of sight of the spectrometer. To accommodate a gradient, the theoretical plasma is divided into zones—each containing the same abundances of each species but each zone is described by a unique temperature and atom number density. In this plasma, radiation from one zone does not effect the atomic populations of another—the justification for this assumption will be discussed in Sec. VIII A. From this assumption, the atomic kinetics of each zone is left uncoupled and can be calculated independently.

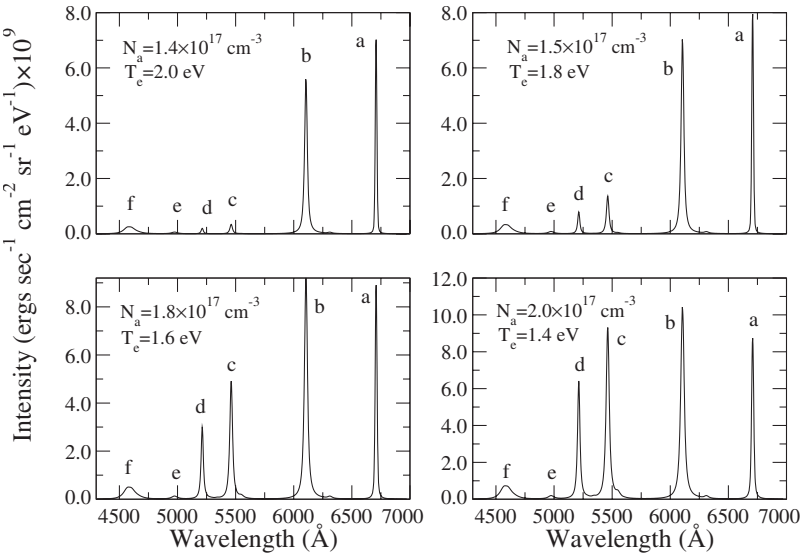

FIG. 12. The effects of temperature on spectra under constant electron density $N_e=2.0\times10^{17}$ cm^{-3}. Labels identifying spectral lines are defined in Table I.

In the ablation plasma under study, the optical depth for emission lines in the same spectrum may vary by several orders of magnitude ($0.4<\tau<400$). This type of variation in the opacity requires a very accurate and numerically stable solution to the radiation transport equation. To this end, a semianalytical solution to the radiation transport equation was developed for this work, the details of which are described in the Appendix.

In addition to solving the traditional transport equation in an accurate manner, a custom nonuniform grid with points concentrated about each emission line was used to more accurately resolve the most optically thick portions of these spectral features.

VII. SYNTHETIC SPECTRA SENSITIVITY IN TEMPERATURE AND DENSITY

This section describes the sensitivity of the synthetic spectra for a plasma uniform in temperature and density. Uniform is understood to be a plasma where the level populations are identical throughout its spatial extent.

To characterize the state of the plasma, a useful spectral region must have spectral features sensitive to both density and temperature. Often a spectral range is chosen to include multiple ionization stages to improve, in particular, the temperature sensitivity, since an increase in temperature drives both population shifts within atoms and in the ionization balance. Here, unfortunately, the line emission of only one ionization stage of either Li or Ag can be clearly discerned.

A. Spectral sensitivity under constant electron density

Figure 12 contains a series of spectra generated with a fixed electron number density of $N_e=2.0\times10^{17}$ cm^{-3} and a decreasing series of temperatures—beginning with $T_e=2.0$ eV and gradually reduced by $\Delta T_e=0.2$ eV. A constant electron density N_e was chosen to eliminate the variations of the emission lines due to changing profiles. Furthermore, a constant N_e reduces the variation in the atomic rates, and in turn, the fractional populations by allowing the rates to vary only by temperature through the rate coefficients. Variation in the atom number density, an outcome of leaving the electron density constant, only affects the absolute and not the relative intensity of an ideal optically thin plasma. The predominant quality seen in this series of plots is the evolution of the heights of Ag lines to a nearly stationary set of Li lines. These spectral characteristics are the effect of both atomic kinetics and opacity.

The behavior of the spectral lines can in part be explained as the effect of the interplay of the two different atomic structures of Li and Ag. The decrease in the magnitude, relative to the Li lines, of the Ag I:$(4d^{10}5d^2$-$4d^{10}5p^2)$ lines is the effect of the increase in temperature driving a shift in population to the higher ionization stages of Ag. The persistence of the Li I:$(1s^23d$-$1s^22p)$ and $(1s^22p$-$1s^22s)$ lines arises from the high (60.9 eV) transition energy to the first excited state of Li^{1+}.

Due to sharp spectral features of Fig. 12, the presence of opacity is not obvious. Figure 13 describes the optical depth associated with each synthetic spectrum of Fig. 12. An overall increase in optical depth is seen to be correlated with a

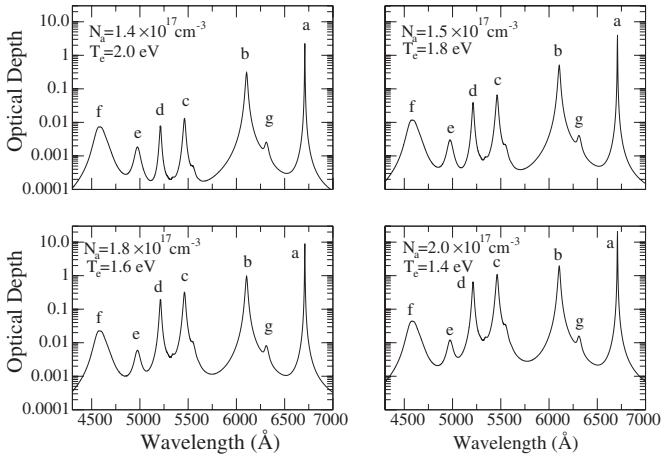

FIG. 13. The corresponding optical depths for constant N_e series.

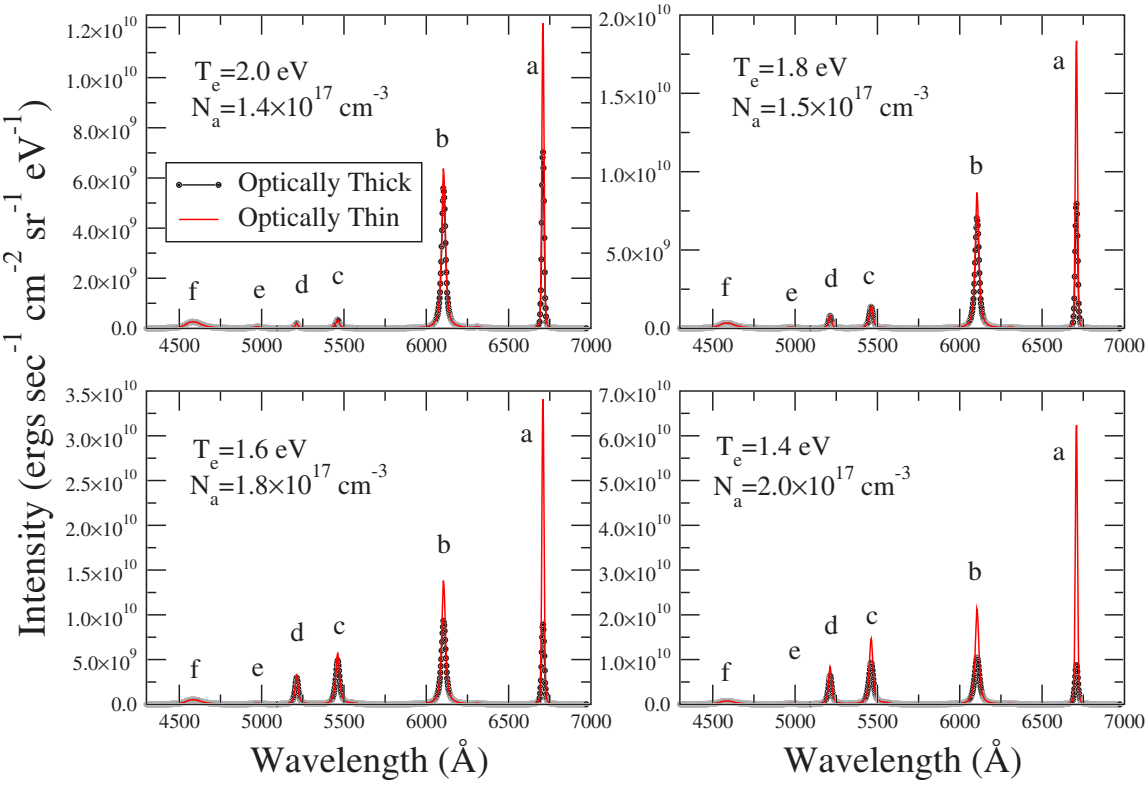

FIG. 14. (Color online) Superposition of optically thin (red lines) and thick (black points) spectra for constant N_e series.

decrease in temperature. This is due to the increase in the total number of absorbers N_a needed to maintain a constant N_e and a shift in population to the lower energy levels of these line transitions. Furthermore, an obvious lack of uniformity in optical depth (τ) is seen across the spectrum with a variation of depths as large as $\Delta\tau=10$ between the Li and Ag lines in the spectrum. The effects of opacity on the spectrum can readily be seen in Fig. 14. Spectra of Fig. 12 are superimposed on spectra generated with the same T_e and N_e, but with the effects of opacity removed.

Opacity reduces the sensitivity of a spectral feature to plasma conditions. This is readily seen in the case of the Li I $2p$-$2s$ and $3d$-$2p$ transitions. A large relative change between the two lines occurs from the $T_e=2.0-1.4$ eV plots for the optically thin spectra, while the optically thick spectra remain relatively unchanged, thus rendering the lithium lines by themselves useless as a diagnostic. The opacity effects in the case of the Li I $2p$-$2s$ line are so extreme in fact that it becomes less dominant than the $3d$-$2p$. Ironically, the weaker Ag lines with their low opacity show the greatest sensitivity for the optically thick system; however, they alone cannot be used as a diagnostic since their relative intensities (ignoring the effects of opacity) are fixed (See Sec. VI A). However, with the Li lines as a reference in conjunction with the Ag lines, a good diagnostic is available at least for temperature.

B. Spectral sensitivity under constant electron temperature

Continuing with the investigation of spectral sensitivity, the emphasis now is on the effects of density. In Fig. 15 a series of synthetic spectra was calculated over one decade of atom number density where the electron temperature was fixed at $T_e=1.4$ eV. See Table III for the associated values of the electron density. This figure displays the increase in spectral intensity for these neutral atomic lines associated with an increase in density. This effect follows from an increase of efficiency in three-body recombination in returning population to the neutral species.

Unlike the previous study at constant N_e, the effect of opacity is clear, in particular for the spectra associated with the highest density. Besides the characteristic self-absorption

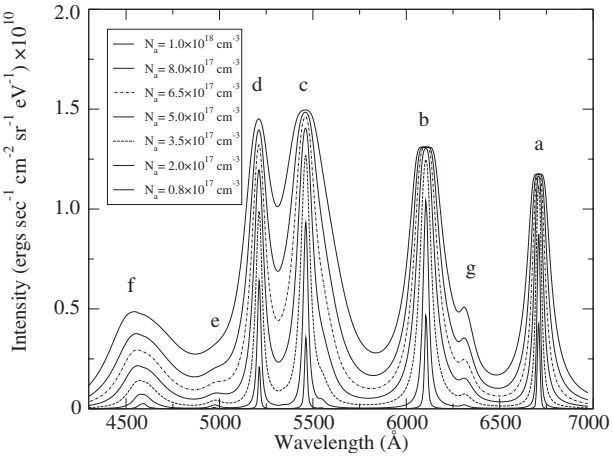

FIG. 15. Synthetic spectra series produced under constant electron temperature, $T_e=1.4$ eV. The corresponding electron densities N_e are given in Table III.

TABLE III. Corresponding electron densities for constant T_e spectral series.

N_a cm^{-3}	N_e cm^{-3}
8.0×10^{16}	8.54×10^{16}
2.0×10^{17}	2.05×10^{17}
3.5×10^{17}	3.51×10^{17}
5.0×10^{17}	4.95×10^{17}
6.5×10^{17}	6.36×10^{17}
8.0×10^{17}	7.76×10^{17}
1.0×10^{18}	9.59×10^{17}

of the two lithium a and b lines in Fig. 15, each individual spectral feature shows a characteristic reduction in the growth of the lines to an upper limit approximating the Planck function. The most optically thick lines reach this limit at lower densities.

Figure 16 displays the optical depth for the corresponding spectra in Fig. 15. For the strongest features, a one decade increase in the atom number density accompanied a one decade increase in the optical depth. In this figure, the clearest evidence of density dependent profiles, with progressively broader features as a function of density, is seen. Interestingly, the increase in atom number density was sufficient to maintain a continual increase in the optical depth, even over the presence of the very sharp line profiles found in the lower densities.

The removal of effects of opacity is shown in Fig. 17. Like the spectra study under constant density, the comparison with the optically thick plasma is striking. The degree of the atomic kinetic effects hidden by opacity becomes apparent: such as the growth of the lithium $2p$-$2s$ (a in Fig. 17) and, to a lesser extent, of the $3d$-$2p$ (b in Fig. 17) lines due to the migration of population from Li^{+1} to neutral lithium.

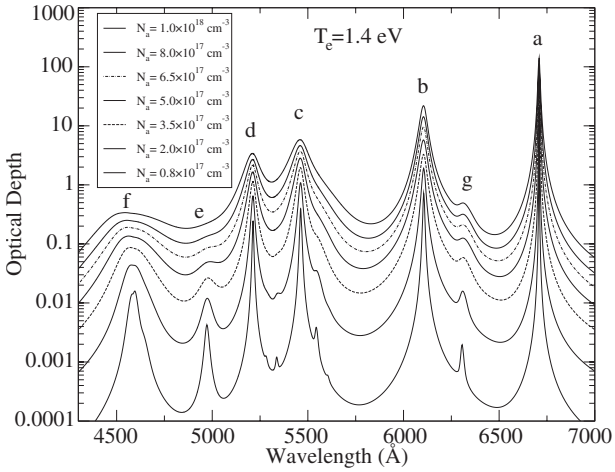

FIG. 16. Optical depths corresponding to constant electron temperature series, $T_e=1.4$ eV. The corresponding electron densities are given in Table III.

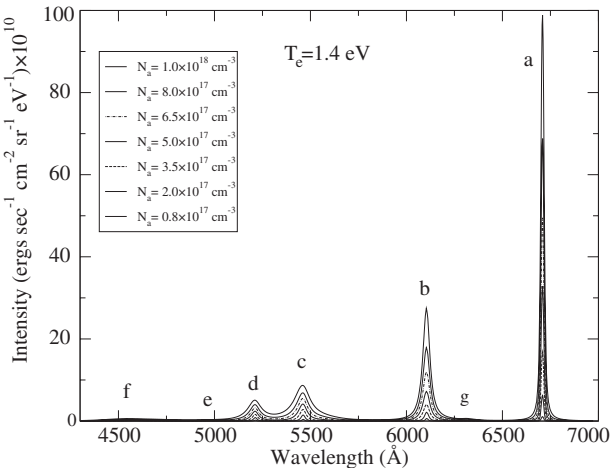

FIG. 17. Optically thin spectra of constant electron temperature series, $T_e=1.4$ eV. The corresponding electron densities are given in Table III.

VIII. THEORY-EXPERIMENT COMPARISON AND DATA ANALYSIS

In this section, four experimental lineouts are compared with synthetic spectra. These four lineouts constitute the earliest spectral data with distinct line emission, and in turn, depict the highest density and temperature plasma conditions of the series of experimental lineouts. Specifically, this data corresponds to the ablated plasma at $t=20$ and 30 ns and at distances from the target surface of 28.8 and 86.4 μm.

A. Self-reversal and the justification of plasma nonuniformity

Until this point the synthetic spectral model has been employed under the uniform slab approximation. This simplest geometry is not burdened by spatial variations in temperature and density and provides a cleaner environment for the interpretation and understanding of the synthetic spectral results. Unfortunately, the self-reversal feature in the Li I: $3d$-$2p$ line suggests the existence of a nonuniform plasma. Though a self-reversal feature may exist in a plasma of uniform density and temperature due to a nonuniformity in level populations arising from a position-dependent radiation field, the plasma referred to in the four lineouts has been shown to be insensitive to the effects of the radiation field on the populations. The effect of the photon field on the populations can be approximated as an effective reduction of the spontaneous radiative decay rate (SRD). This approximation is the basis for the use of escape factors [26] to include the effects of radiation in atomic kinetic models. A test conducted with the atomic kinetic model for the relevant densities and temperatures predicted for the four early in time lineouts showed no variation in level populations when the SRD rate was eliminated.

B. Temperature and density spatial profile generation

To simulate a nonuniform plasma, a series of temperature and density profiles that define the search space must be generated. The process begins by selecting the set of T_e and

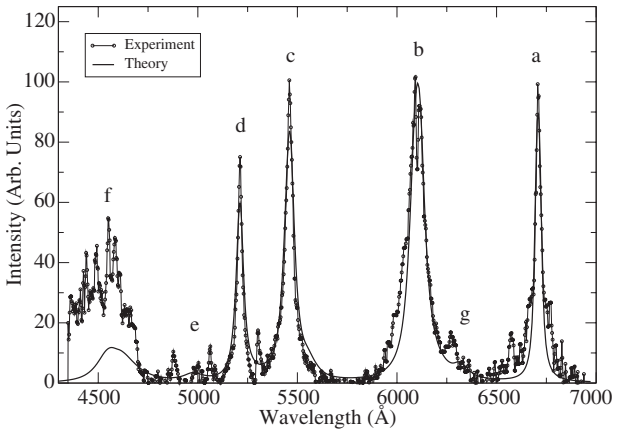

FIG. 18. Experimental lineout at $x=28.8$ μm and $t=20$ ns with predicted $T_e=1.5$ eV and $N_a=4.0\times10^{17}$ cm^{-3} uniform synthetic spectra.

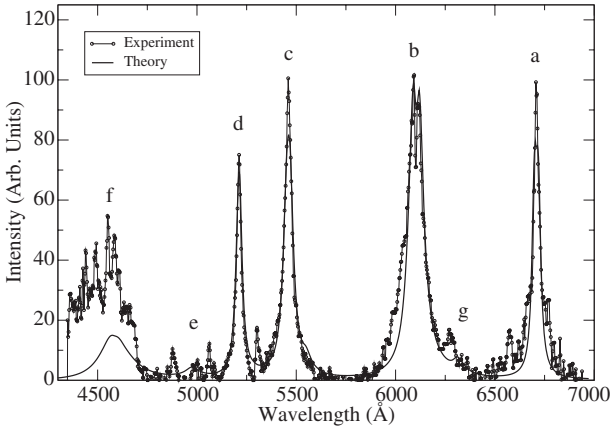

FIG. 19. Experimental lineout at $x=28.8$ μm and $t=20$ ns with predicted $T_e=[1.1,1.9,1.9,1.1]$ eV and $N_a=[2.5,4.5,4.5,2.5]\times10^{17}$ cm^{-3} four-zone synthetic spectra.

N_a available to any spatial zone. The profiles were then constrained to be symmetric with respect to the center and so that the two center zones contain the maximum values: this means that a zone may take on values equal to or less than its neighbor who resides in the direction toward the center of the profile. In other words, profiles are either uniform or a approximate concave-down function. Following these restrictions, an exhaustive generation of the profiles was performed. The requirement of spatial zones of uniform width was a further restriction placed on the model.

C. Trial description

Each synthetic spectrum generated was compared with an experimental lineout to determine the best least-squares fit. Three trials were performed for the set of two experimental lineouts—they included a uniform, four- and six-spatial zone simulations.

The following are the three trial series for the comparison with $t=+20$ ns and $t=+30$ ns, both at $x=28.8$ μm lineouts. Results for the $x=86.4$ μm lineouts follow in a similar manner.

In the comparison shown in Fig. 18, both the $t=20$ ns lineouts proved to be the most difficult to model. The existence of contamination along the wings of the main spectral features, in conjunction with an asymmetry on the high-energy side of the Li I: $3d$-$2p$ line feature, hindered the comparison. Interestingly, the single zone calculation obtains the main characteristics of the spectrum. Due to the uniform radiation transport calculation, the Li I: $3d$-$2p$ self-reversal cannot be approximated nor can the slight asymmetry about the self-reversal.

Even with the difficulties mentioned above, the four-zone calculation shows improvement, as shown in Fig. 19. The self-reversal and the slight asymmetry have now become apparent in the synthetic spectrum with the inclusion of the gradient. Line profiles for the most part compare relatively well for the broadest portions of the spectral lines. Platinum contamination in the silver (c in Fig. 19) and lithium (b in Fig. 19) lines may partially explain the discrepancy between the spectra.

For the six-zone calculation, shown in Fig. 20, the improvement in the numerical fitness unfortunately does not follow an obvious improvement in the spectral comparison. This lack of real improvement may be due to the limits of the use of a low number of uniform zones in the radiation transport calculation. Another possible remedy to improve the comparison in the heights would be to employ a nonuniform grid for the inclusion of narrower zones at the perimeter, to contribute low density spectral emission without including their characteristic high opacity. Unfortunately, a scheme has not been devised to confidently search through such a large domain that a variable width spatial grid would entail.

As mentioned above, part of the difficulty in the comparison arises from an asymmetry in the high-energy side of the Li I: $3d$-$2p$ line (d in Fig. 20). The existence of this feature has several possible explanations. Oxidation of the target after fabrication, in particular with lithium atoms, was concluded to be the origin of Li_2O and LiOH molecules found in the target. The strong $2s^22p^33p\ ^5P$-$2s^22p^34d\ ^5D$ and $2s^22p^33p\ ^3P$-$2s^22p^36p\ ^3S$ transitions of neutral oxygen are found in this location, as well as other strong transitions on the high-energy side of the Li (a in Fig. 20) line where contamination is found.

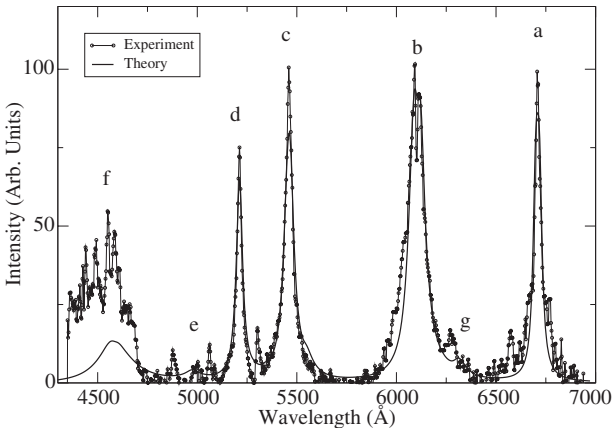

FIG. 20. Experimental lineout at $x=28.8$ μm and $t=20$ ns with predicted $T_e=[1.2,1.2,2.0,2.0,1.2,1.2]$ eV and $N_a=[2.0,3.5,6.0,6.0,3.5,2.0]\times10^{17}$ cm^{-3} six-zone synthetic spectra.

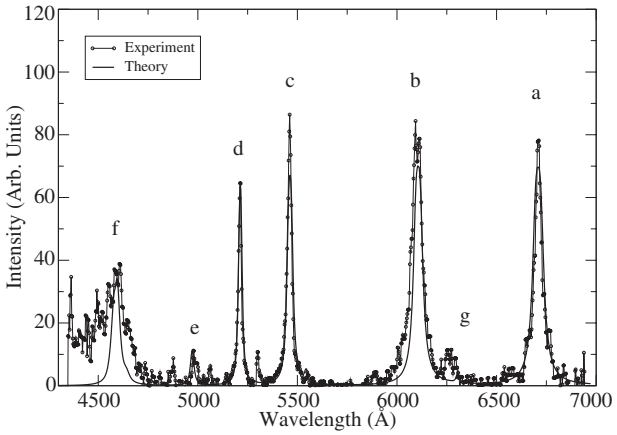

FIG. 21. Experimental lineout at $x=28.8$ μm and $t=30$ ns with predicted $T_e=0.8$ eV and $N_a=1.0\times10^{17}$ cm^{-3} uniform synthetic spectra.

Another possible explanation is the effects of Li^{+0}-Li^{+0}, Li^{+0}-Ag^{+0}, and/or Li^{+0} molecule interactions for the broadening of the spectral line. Estimates based on Ref. [26], for resonance (line broadening between levels of the same species connected by a dipole transition) and van der Waals (more general atom-atom interaction) broadening were found to be small in comparison to Stark broadening. It should be kept in mind that limitations to these approximations exist, and in particular for Li^{+0}-Ag^{+0} broadening these estimates may not be appropriate.

Due to the possibility of contamination and the plasma's high opacity, developing and performing more sophisticated profile calculations with the hopes of explaining the asymmetry would be impractical.

The comparison with the synthetic spectra for the $t=+30$ ns, $x=28.8$ μm appears much better than the $t=+20$ ns data. The asymmetry no longer dominates the high-energy side of the $3d$-$2p$ line, and the existence of contaminating features appears to be weaker about the wings of the main features. The uniform calculation, Fig. 21, captures most of the main features; however, the Li I: $3d$-$2p$ line width is underestimated. As a confirmation of the quality of the comparison, the Li I: $4s$-$2p$ and $4d$-$2p$ lines found in the f (in Fig. 21) complex of lines compares well with the experimental data though they have not been included in the least-squares minimization procedure.

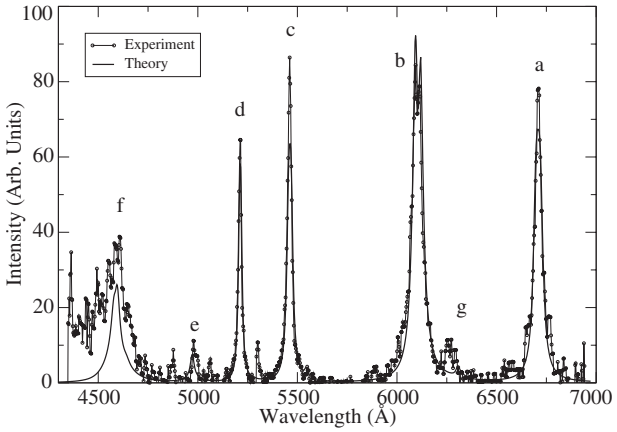

FIG. 22. Experimental lineout at $x=28.8$ μm and $t=30$ ns with predicted $T_e=[0.7,1.8,1.8,0.7]$ eV and $N_a=[1.0,2.0,2.0,1.0]\times10^{17}$ cm^{-3} four-zone synthetic spectra.

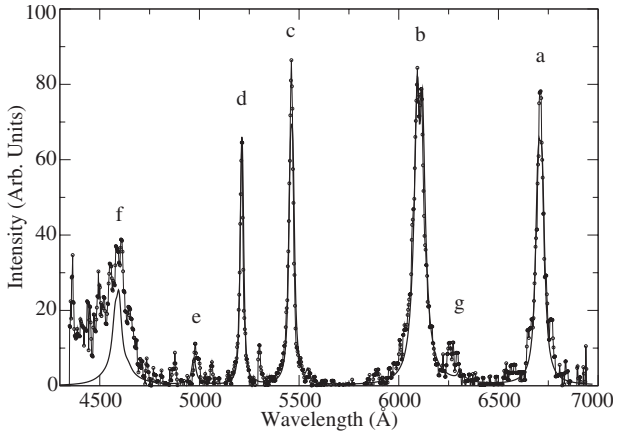

FIG. 23. Experimental lineout at $x=28.8$ μm and $t=30$ ns with predicted $T_e=[0.7,0.8,2.3,2.3,0.8,0.7]$ eV and $N_a=[1.0,1.0,2.5,2.5,1.0,1.0]\times10^{17}$ cm^{-3} six-zone synthetic spectra.

In the four-zone calculation, Fig. 22, the self-reversal on line b is clearly displayed, and also a much better agreement in the width of the Li I: $3d$-$2p$ line is observed. For the six-zone case, Fig. 23, the comparison is quite favorable. Again platinum lines in c and a (in Fig. 23) contribute to the disparity.

Figure 24 describes the optical depth of the six-zone synthetic spectra. Notice that the optical depth is greater for the $t=+30$ ns series at the line center while between the spectral features the opacity is much lower. This quality of high variation in the optical depth from line center to spectral valley is due to the existence of very sharp line profiles in the Li I: $2s$-$2p$ and $3d$-$2p$ lines that are associated with the low electron density. Also, lower temperatures are found in the $t=+30$ ns spectra that place more population in the lower levels of the line transitions. Notice in this figure that the silver lines approach optical depths as high as $\tau=10$, while the Li I: $2s$-$2p$ has $\tau=400$. Interestingly, the uniform and four-zone optical depths are similar to the six-zone case.

Figures 25 and 26 describe the one, four, and six zone resulting profiles for the $t=+20$ and $+30$ ns calculations, respectively.[6] The $t=+30$ ns results show distinct differences in boundary and core values, where the single zone solution consistently approximates the boundary values for both T_e and N_a. These two boundary zones predominantly contribute to the nonuniform opacity needed to reduce Li I [a and b (in Fig. 24)] lines with respect to the Ag I [c and d (in Fig. 24)] lines, while the higher density core provides the higher electron density needed to match the widths of the spectral lines. For the $t=+20$ ns results, the single zone solution appears to approximate the average of the entire profile. This implies that all zones are strongly participating in the opacity and in

[6]Interestingly, 1D hydrodynamic results discussed earlier produced a similar prediction of the temperature and density to that of the uniform results to within a factor of 3.

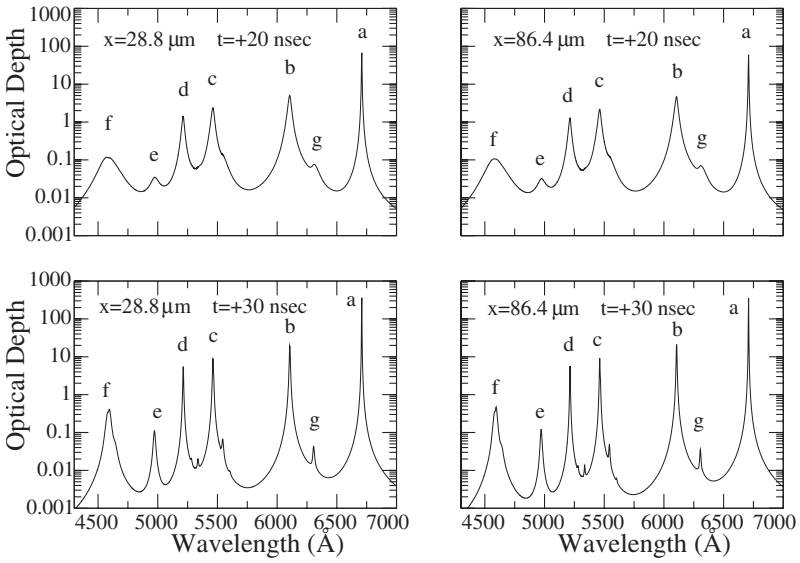

FIG. 24. Optical depths obtained from six-zone synthetic spectra model for $t=+20$ ns, $x=28$ μm, and $x=86.4$ μm; and $t=+30$ ns, $x=28$ μm, and $x=86.4$ μm experimental lineouts.

the line broadening. Therefore, spectral line widths are not primarily defined by any particular region of the plasma, unlike the previous results.

D. Lithium lines behavior under high opacity

We conclude this section by describing the difference in behavior of the Li I:3*d*-2*p* and 2*p*-2*s* lines. One critical question arises about the behavior of these lines: If the Li I:2*s*-2*p* line has the largest optical depth, then why is a large self-reversal not present in the line, such as that found in the Li I:3*d*-2*p* line? The answer lies in the emissivity and opacity functions. From Fig. 27 we see that the Li I:3*d*-2*p* (b) line is composed of contributions from different spatial regions of the plasma: the wings of the line originate from the high density center region of the plasma, while the core of the line originates from the low density spatial region of the plume. This configuration is optimal for a self-reversal in particular for a plasma of large spatial extent. In other words, we may consider the core of the line approaching the Planckian function at a different temperature than that of the wings. On the other hand, the Li I:2*s*-2*p* line is not dominated by contributions from different plasma regions: its line profile is dominated by emission and absorption from the boundaries of the plasma. Therefore, this line behaves as if it were produced from a uniform plasma simply undergoing self-absorption without significant self-reversal.

IX. SUMMARY

This work has addressed the spectroscopic analysis of low fluence laser driven ablation plasmas of the kind found in typical laser-ablation applications of material synthesis and

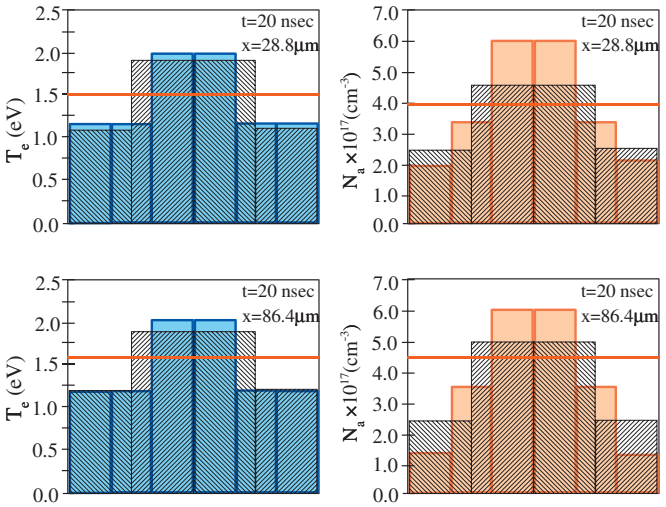

FIG. 25. (Color) T_e and N_a profiles obtained by comparing the $t=+20$ ns, $x=28\mu$m, and $x=86.4$ μm experimental lineouts with the following three synthetic spectral models: the uniform model (represented by the red horizontal line), the four-zone model (diagonally hatched boxes), and the six-zone model (filled color boxes).

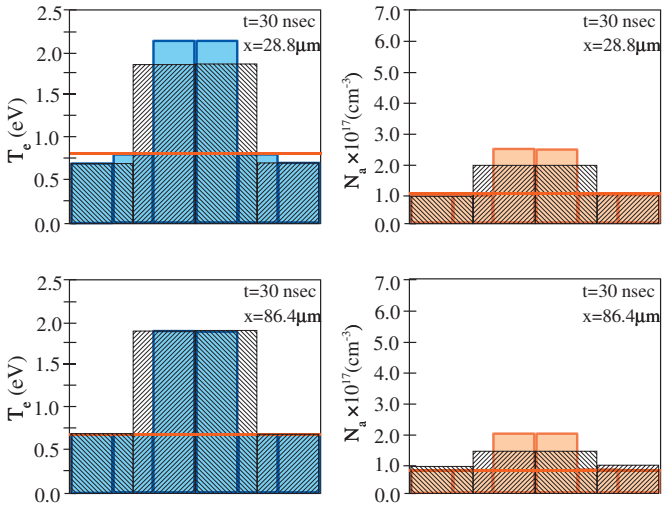

FIG. 26. (Color) T_e and N_a profiles obtained by comparing the $t=+30$ ns, $x=28$ μm, and $x=86.4$ μm experimental lineouts with the following three synthetic spectral models: the uniform model (represented by the red horizontal line), the four-zone model (diagonally hatched boxes), and the six-zone model (filled color boxes).

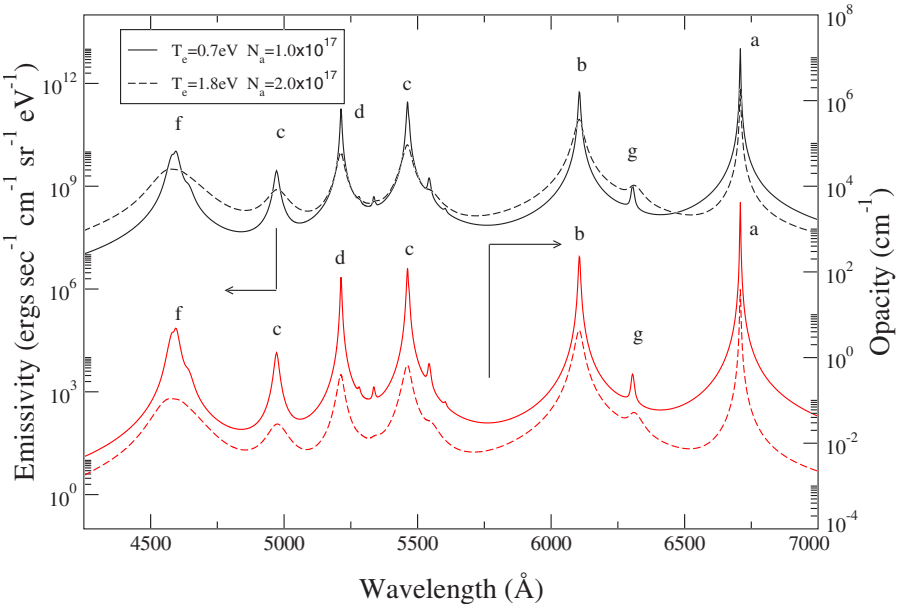

FIG. 27. (Color online) Four-zone emissivity (the two upper curves and associated left-hand y axis) and opacity (the two lower curves and associated right-hand y axis) from $t=+30$ ns, $x=28.8$ μm synthetic spectra results from plasma core and boundary zones ($T_e=[0.7,1.8,1.8,0.7]$ eV and $N_a=[1.0,2.0,2.0,1.0]\times 10^{17}$ cm^{-3}).

thin film manufacturing. Efforts concentrated on developing techniques to quantitatively model this complex environment. These modeling techniques were applied to the analysis of a collisionally confining laser-ablation experiment designed to reduce lateral plasma gradients to aid in spectroscopic characterization of the plume.

The specific modeling techniques developed to generate synthetic spectra in this regime include applying a semiempirical technique to correct the energy level structure of neutral and near neutral high-Z elements; developing a multielement collisional-radiative atomic kinetic model that solves self-consistently the level populations of all participating atoms and ions with the shared pool of free electrons; developing a procedure for producing detailed line shapes tailored for neutral and near neutral species; and developing an accurate radiation transport model to properly account for the larger variation of optical depth affecting the different spectral lines in the emission spectra.

This model revealed the significance of opacity on the emission spectra. In addition, this analysis revealed the role of plasma gradients in the shape of the spectral features and provided an explanation for the observed self-reversal in the less optically thick Li:$3d$-$2p$ line as opposed to the Li:$2p$-$2s$ line.

The techniques developed in this work are general and may be applied to the analysis of more stoichiometrically complex, steady state plasma plumes.

ACKNOWLEDGMENTS

This work was supported by NSF Grant No. OSR-9353227, and by the UCCSN.

APPENDIX: SEMIANALYTICAL SOLUTION TO THE RADIATION TRANSPORT EQUATION

As mentioned in Sec. VI B, the larger variation in the optical depth of the various emission lines in the Li-Ag spectra requires an accurate and numerically stable solution to the radiation transport equation. This appendix describes the formalism of the semianalytical solution to the radiation transport equation developed for this work.

The transport of radiation in slab geometry is described by the following equation:

$$\mu\frac{dI_{\nu\mu}}{dz} = -k_\nu(z)I_{\nu\mu}(z) + j_\nu(z), \quad \mu=\cos\theta, \tag{A1}$$

where I_ν is the spectral intensity between ν and $d\nu$ (in units of ergs s^{-1} cm^{-2} steradians^{-1} Hz^{-1}); j_ν (in units of ergs s^{-1} cm^{-3} steradians^{-1} Hz^{-1}) and k_ν (in units of cm^{-1}) are the spectral emission coefficient and spectral linear absorption coefficient (opacity), respectively. Consider a transition between an upper level i and a lower level k. Then, the spectral emissivity may be written as

$$j_\nu = \sum_{i=1}^{n_l}\sum_{k<i} n_i A_{ik}\{\phi_{ik}\}_\nu \frac{h\nu_{ik}^0}{4\pi}, \tag{A2}$$

where A_{ik} is the spontaneous radiative decay (in units of s^{-1}), n_i is the particle number density (in units of cm^{-3}), and ϕ_{ik} (in units of Hz^{-1}) is the line profile associated with the i to j transition and satisfies the normalization condition $\int\phi_{ik}d\nu=1$. The opacity may be written as

$$k_\nu = \sum_{i=1}^{n_l}\sum_{k>i} (n_i B_{ik} - n_k B_{ki})\{\phi_{ik}\}_\nu \frac{h\nu_{ik}^0}{4\pi}, \tag{A3}$$

where both B_{ik}, the stimulated emission coefficient, and B_{ki}, the photoabsorption coefficient, are in units of cm^2 ergs^{-1} Hz. From Eq. (A1) the spectral intensity for a plasma in slab geometry as a function of the position L in the plasma with no backlighter can be written as

$$I_{\nu\mu}(L) = \int_0^L \exp[-\tau_\nu(t)] j_\nu(t) dt, \tag{A4}$$

where the optical depth $\tau_\nu(t) = \int_t^L k_\nu(t')dt'$. To solve for $I_{\nu\mu}(L)$, the outer integral of Eq. (A4) was discretized resulting in

$$I_{\nu\mu}(L) = \sum_{i=1}^{N} \int_{t_i}^{t_{i+1}} \exp[-\tau_{\nu i}(t)] j_{\nu i}(t) dt. \tag{A5}$$

If the spatial discretization of the plasma along the line of sight is fine enough such that both the emissivity and the optical depth may be considered linear within each spatial zone i, then Eq. (A5) may be written as

$$I_{\nu\mu}(L) = \sum_{i=1}^{N} \int_{t_i}^{t_{i+1}} \exp[-(\alpha_i + \beta_i t)_{\tau,\nu}](a_i + b_i t)_{j,\nu} dt. \tag{A6}$$

For each spatial zone i, the integral may be evaluated analytically to obtain Eq. (A7),

$$I_{\nu\mu}(L) = \sum_{i=1}^{N} \left\{ \frac{1}{\beta_i} \exp[-(\alpha_i + \beta_i t_{i+1})] \times \left[\left(a_i + b_i x_i + \frac{b_i}{\beta_i} \right) \exp[\beta_i (t_{i+1} - t_i)] - \left(a_i + b_i t_{i+1} + \frac{b_i}{\beta_i} \right) \right] \right\}. \tag{A7}$$

The model developed from this technique was compared to the uniform slab solution, $I = \frac{j_\mu}{k_\mu}[1 - \exp(-k_\mu L)]$ for the same 10 zone Li-Ag plasma with a $T_e = 0.7$ eV and a $N_a = 1.0 \times 10^{17}$ cm^3 for various plasma thicknesses ranging from 0.01 cm to 100 cm. For the case of the thickest plasma, optical depths at line centers ranged from 10 000 to 100 000. The results from the two models were graphically indistinguishable.

[1] *Laser-Induced Plasmas and Applications*, edited by L. J. Radziemski and D. A. Cremers (Marcel Dekker, New York, 1989), pp. 1–67.

[2] D. B. Chrisey and G. K. Hubler, *Pulsed Laser Deposition of Thin Films* (Wiley-Interscience, New York, 1994).

[3] H. M. Smith and A. F. Turner, Appl. Opt. **4**, 147 (1965).

[4] P. Lorazo, L. J. Lewis, and M. Meunier, Proc. SPIE **4276**, 57 (2001).

[5] K. R. Chen, J. N. Leboeuf, R. F. Wood, D. B. Geohegan, J. M. Donato, C. L. Liu, and A. A. Puretzky, Phys. Rev. Lett. **75**, 4706 (1995).

[6] R. F. Wood, K. R. Chen, J. N. Leboeuf, A. A. Puretzky, and D. B. Geohegan, Phys. Rev. Lett. **79**, 1571 (1997).

[7] R. F. Wood, J. N. Leboeuf, D. B. Geohegan, A. A. Puretzky, and K. R. Chen, Phys. Rev. B **58**, 1533 (1998).

[8] R. F. Wood, J. N. Leboeuf, K. R. Chen, D. B. Geohegan, and A. A. Puretzky, Appl. Surf. Sci. **127–129**, 151 (1998).

[9] *Laser Ablation and Desorption*, edited by J. C. Miller and R. F. Haglund (Academic, New York, 1998), pp. 255–289.

[10] H. R. Griem, Phys. Fluids B **4**, 2346 (1992).

[11] M. J. Herbst, P. G. Burkhalter, J. Grun, R. R. Whitlock, and M. Fink, Rev. Sci. Instrum. **53**, 1418 (1982).

[12] C. E. Moore, *Bibliography on the Analyses of Optical Atomic Spectra*, U.S. National Bureau of Standards Special Publication 306 (National Bureau of Standards, Washington, DC, 1968).

[13] J. Pickering and V. Zillio, Eur. Phys. J. D **13**, 181 (2001).

[14] J. Abdallah, Jr., R. E. H. Clark, and R. D. Cowan, Theoretical atomic physics code development Vol. I CATS: Cowan Atomic Structure Code, Los Alamos National Laboratory Report LA-11436–M, December 1988 (unpublished).

[15] R. D. Cowan, *The Theory of Atomic Structure and Spectra* (University of California, California, 1981).

[16] R. E. H. Clark, Joseph Abdallah, Jr., George Csanak, Joseph Mann, and Robert D. Cowan, Theoretical atomic physics code development Vol. II ACE: Another collisional excitation code, Los Alamos National Laboratory Report LA-11436–M, December 1988 (unpublished).

[17] M. E. Sherrill, R. C. Mancini, J. E. Bailey, A. Filuk, B. Clark, P. Lake, and J. J. Abdallah, Rev. Sci. Instrum. **72**, 957 (2001).

[18] A. Burgess, Astrophys. J. **141**, 1588 (1965).

[19] Y. P. Raizer, Sov. Phys. Usp. **8**, 650 (1966).

[20] J. C. Stewart and K. D. Pyatt, Astrophys. J. **144**, 1203 (1966).

[21] R. M. More, Atomic physics in inertial confinement fusion, Lawrence Livermore National Laboratory Report UCRL-84991, March 1981 (unpublished).

[22] L. A. Woltz and C. F. J. Hooper, Phys. Rev. A **38**, 4766 (1988).

[23] R. C. Mancini, D. P. Kilcrease, L. Woltz, and C. F. J. Hooper, Comput. Phys. Commun. **63**, 314 (1991).

[24] C. A. Iglesias, H. E. DeWitt, J. L. Lebowitz, D. MacGowan, and W. B. Hubbard, Phys. Rev. A **31**, 1698 (1985).

[25] R. J. Tighe and C. F. J. Hooper, Phys. Rev. A **15**, 1773 (1977).

[26] H. R. Griem, *Principles of Plasma Spectroscopy* (Cambridge University Press, Cambridge, 1997).